

## Supporting Information

### A core-shell electrode for dynamically and statically stable Li-S battery chemistry

Sheng-Heng Chung, Chi-Hao Chang, and Arumugam Manthiram \*

*Materials Science and Engineering Program & Texas Materials Institute  
The University of Texas at Austin, Austin, TX 78712, USA*

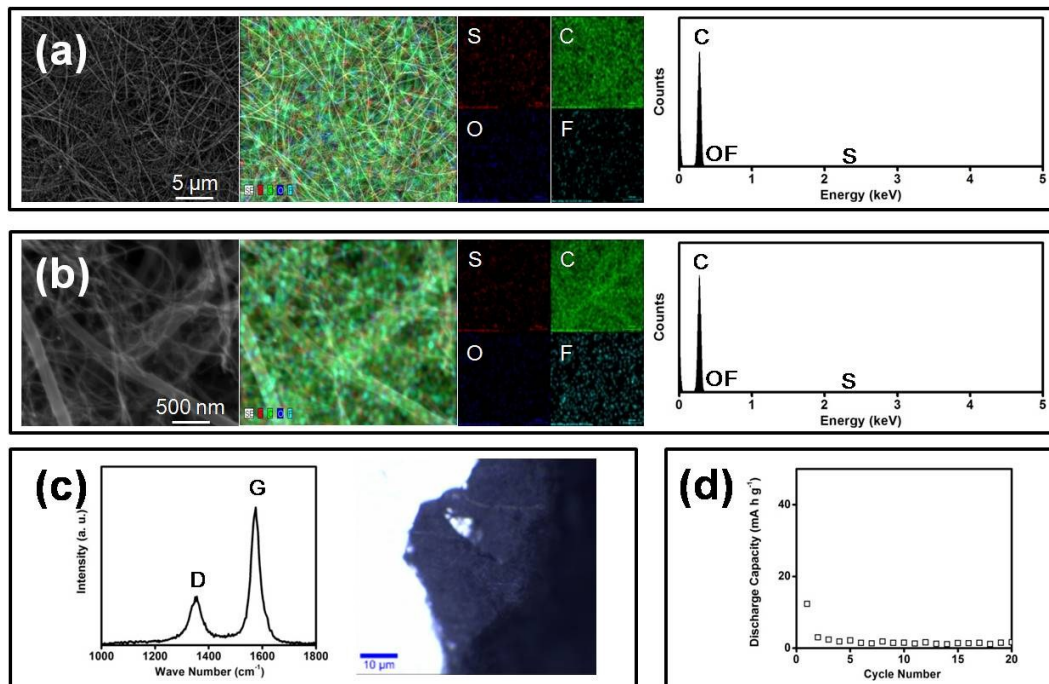


Fig. S1. Physical and chemical analyses of the carbon paper: (a, b) low and high magnification SEM/EDX inspections, (c) Raman spectrum, and (d) electrochemical characteristics.

SEM/EDX inspections demonstrate that the commercial carbon paper consists of a CNT/CNF composite network. The interwoven CNTs are entangled in the long-range CNF framework, which builds up a continuous electron pathway and a successive electrolyte channels. Raman spectrum shows a high intensity ratio of G band to D band. The high graphitization level of the carbon paper indicates the fast electron-transfer capability. The cycling performance of the carbon paper indicates its high electrochemical and chemical stability in a Li-S electrochemical cell.

Moreover, in order to focus on the effect of the core-shell cathode configuration, the commercial carbon paper that is used in this study has a low specific surface area (81 m<sup>2</sup> g<sup>-1</sup>) and no micropores. This excludes any significant contributions that may arise from porous carbon characteristics.

\*Corresponding author. Tel: +1-512-471-1791; fax: +1-512-471-7681.

*E-mail address:* manth@austin.utexas.edu (A. Manthiram)

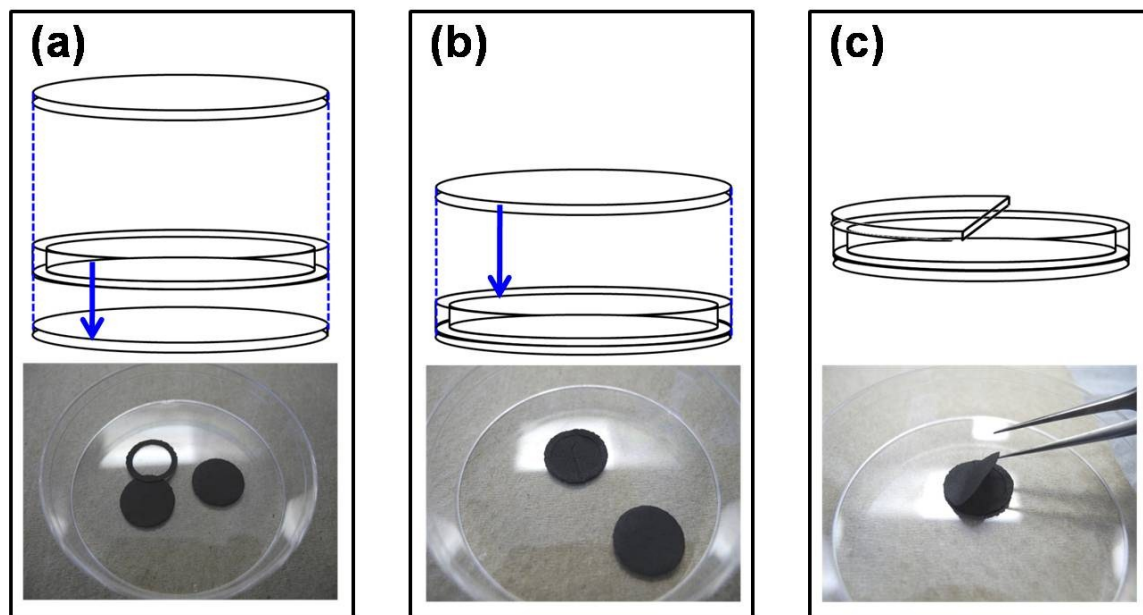


Fig. S2. Configuration of the shell-shaped carbon electrode: schematics of the parts and the corresponding digital images of the shell-shaped electrode.

The parts drawings shown in Fig. S2 illustrate step-by-step the fabrication of the core-shell cathode. Fig. S2a shows the cell components made by the commercial carbon paper (proprietary MWCNT Blend, Nano Tech Labs). The carbon papers are cut into circular disks with the area and diameter of, respectively,  $1 \text{ cm}^2$  and  $\sim 1.13 \text{ cm}$ . The circular carbon papers are configured as the upper and lower electrode shells. The carbon o-ring is made from the same carbon paper with the inside diameter of  $\sim 0.95 \text{ cm}$ . Fig. S2b shows the first step for fabricating the shell-shaped cathode. The carbon o-ring is directly pressed onto the lower carbon shell, which creates a porous space in the middle of the carbon electrode. The porous space is ready for the addition of the sulfur core during cell fabrication. Finally, the upper carbon shell is covered on the top for the purpose of shielding the sulfur core, as show in Fig. S2c. The commercial carbon paper consists of interwoven CNT/CNF networks and, therefore, the use of binder is unnecessary. By utilizing this characteristic, the above-mentioned three cell components are able to build up the shell-shaped electrode by simply pressing.

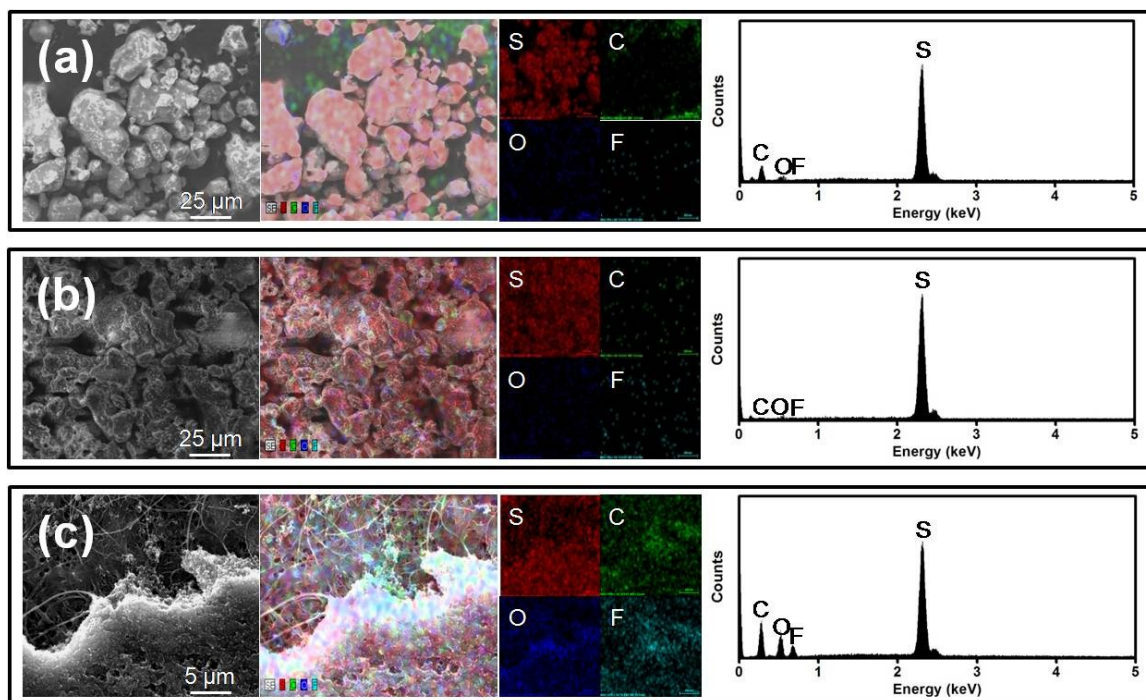


Fig. S3. Microstructural analysis: SEM/EDX inspection of the (a) commercial sulfur powder, (b) uncycled sulfur core, and (c) cycled sulfur core.

In Fig. S3a, the commercial sulfur powder (Alfa Aesar; 325 mesh, 99.5%) shows agglomerated particles and clusters with a particle size larger than 50  $\mu\text{m}$ . Although pure sulfur powders are safe, cost-effective, and environmentally benign cathode materials, such large particles increase the cathode resistance and reduce the electrochemical activity. Thus, a new customized cathode configuration would be a possible solution to allow the successful usage of micron-sized sulfur powders directly as a low-cost active material. Fig. S3b and c shows the sulfur core before and after cycling. The obvious sulfur clusters and the strong elemental sulfur signals in the EDX mapping results provide solid evidence that the sulfur core is well stabilized within the shell-shaped electrode during electrochemical cycling.

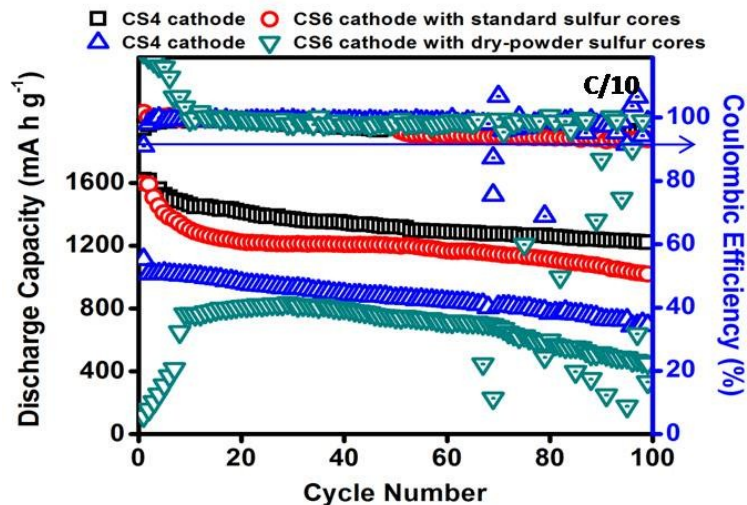


Fig. S4. Configuration of the core-shell cathode: battery performance of the core-shell cathodes with standard sulfur cores and dry-powder sulfur cores.

Two different sulfur cores were encapsulated into the shell-shaped electrodes for investigating the electrochemical characteristics, as shown in Fig. S4. The standard sulfur cores were prepared by dispersing micron-sized sulfur powder in a blank electrolyte for 10 min. The cloudy suspension was subsequently added into the porous space of the shell-shaped electrode. The dry-powder sulfur cores were prepared by directly using dry sulfur powder as the sulfur core. The electrolyte was added after the preparation of the core-shell cathodes. The core-shell cathodes employing these two sulfur cores were controlled to have the same cell composition and measured under the same condition.

The comparative experiment shows that the cells using the dry-powder sulfur cores have a relatively low electrochemical utilization and charge/discharge efficiency as compared to the cells employing the standard sulfur cores. Moreover, as the sulfur loading increases to  $6 \text{ mg cm}^{-2}$ , the dry-powder sulfur cores need a long activation process to attain their peak capacity and subsequently become unstable. The poor cell performance of the dry-powder sulfur cores might result from that the inner sulfur may not be wetted by the electrolyte and cannot be well utilized. These inactive sulfur clusters sitting inside the dry-powder sulfur cores increase the cathode resistance and, therefore, lower the overall cell performance.

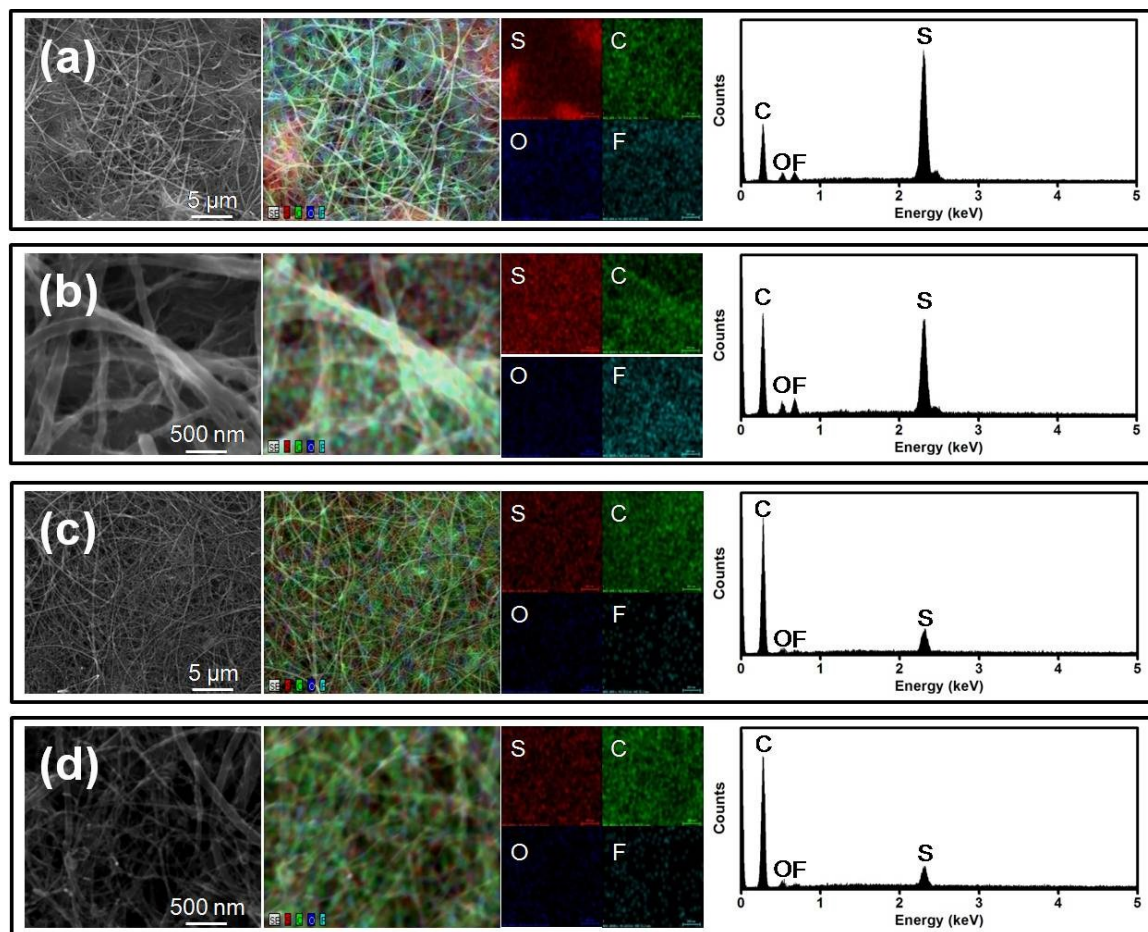


Fig. S5. Microstructural analysis: (a, b) low and high magnification SEM/EDX inspection at the center area of the uncycled core-shell cathodes and (c, d) low and high magnification SEM/EDX inspection from the edge of the uncycled core-shell cathodes. The uncycled core-shell cathodes shown in Fig. S5 have a  $4 \text{ mg cm}^{-2}$  sulfur core. The microstructural analysis is conducted after the cathodes have been rested for 6 h.

The surface SEM/EDX inspection at the center area and from the edge of the uncycled core-shell cathode exhibits the sulfur clusters (SEM images) and strong elemental sulfur signals (EDX analyses) only inside of the core-shell cathodes.

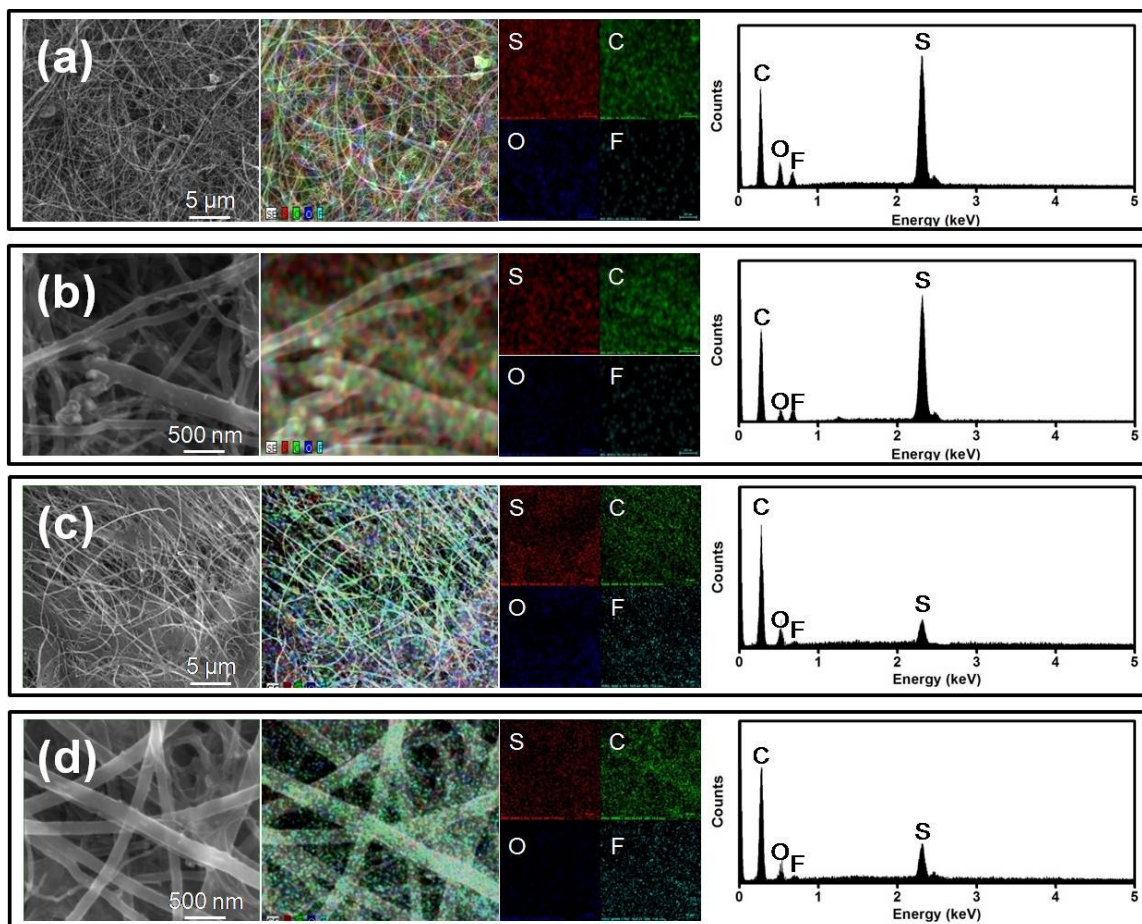


Fig. S6. Microstructural analysis: (a, b) low and high magnification SEM/EDX inspection at the center area of the cycled core-shell cathodes and (c, d) low and high magnification SEM/EDX inspection from the edge of the cycled core-shell cathodes. The cycled core-shell cathodes in Fig. S6 have a  $4 \text{ mg cm}^{-2}$  sulfur core. The microstructural analysis is conducted after the cathodes have been cycled for 100 cycles and stopped at the charged state (3.0 V).

After cycling, the core-shell cathodes show (i) strong elemental sulfur signals and unchanged CNT/CNF morphology at the center area and (ii) limited elemental sulfur signals from the edge. These features demonstrate that the shell-shaped electrode could cease the severe polysulfide diffusion.

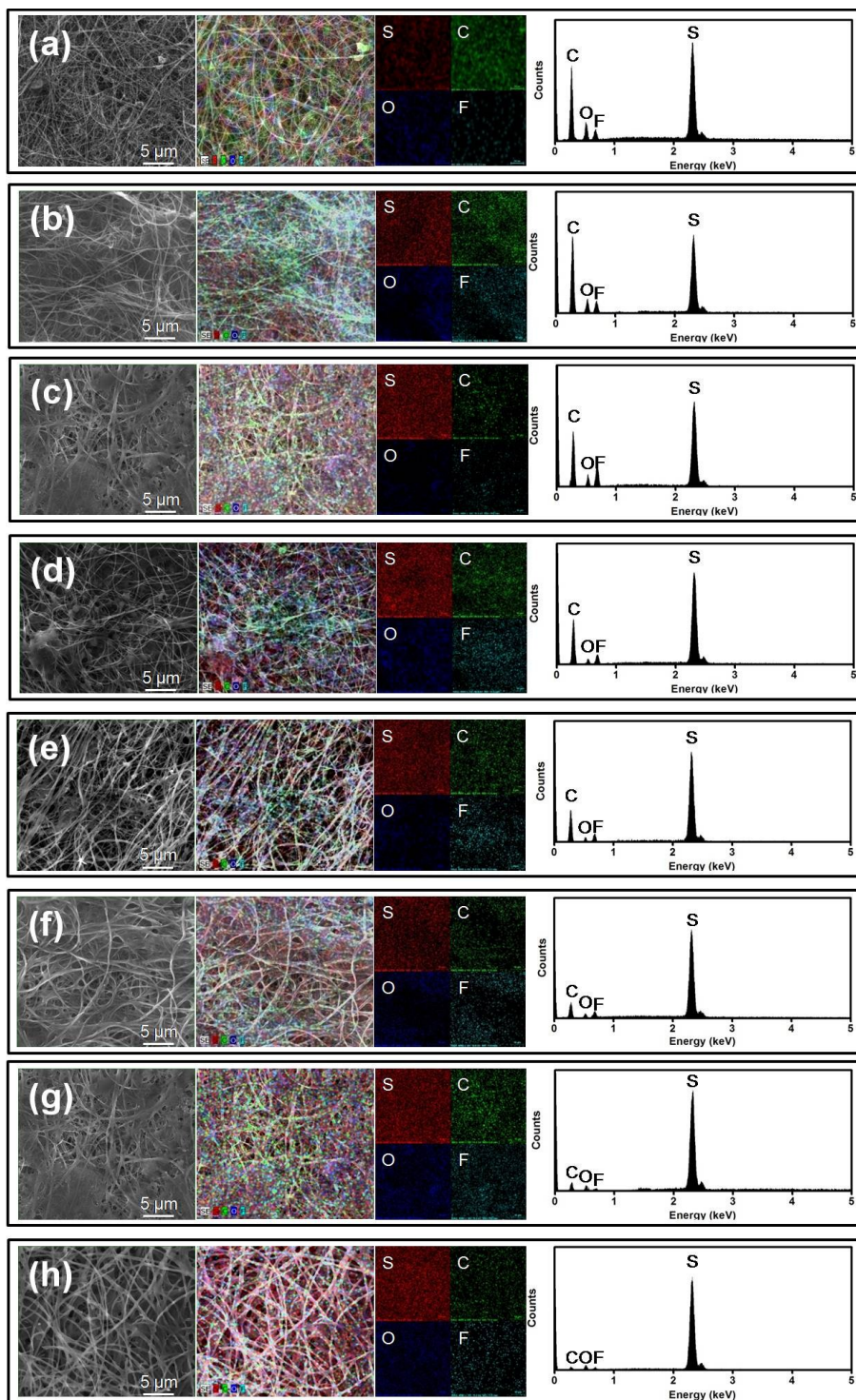


Fig. S7. Microstructural analysis: SEM/EDX inspection from the surface layer of the cyclized core-shell cathodes with (a)  $4 \text{ mg cm}^{-2}$ , (b)  $6 \text{ mg cm}^{-2}$ , (c)  $8 \text{ mg cm}^{-2}$ , (d)  $10 \text{ mg cm}^{-2}$ , (e)  $20 \text{ mg cm}^{-2}$ , and (f)  $30 \text{ mg cm}^{-2}$  sulfur cores; and SEM/EDX inspection from the inner layer of the cyclized core-shell cathodes with (g)  $4 \text{ mg cm}^{-2}$  and (h)  $30 \text{ mg cm}^{-2}$  sulfur cores. The microstructural analysis is conducted after the cathodes have been cycled for 100 cycles and stopped at the charged state (3.0 V).

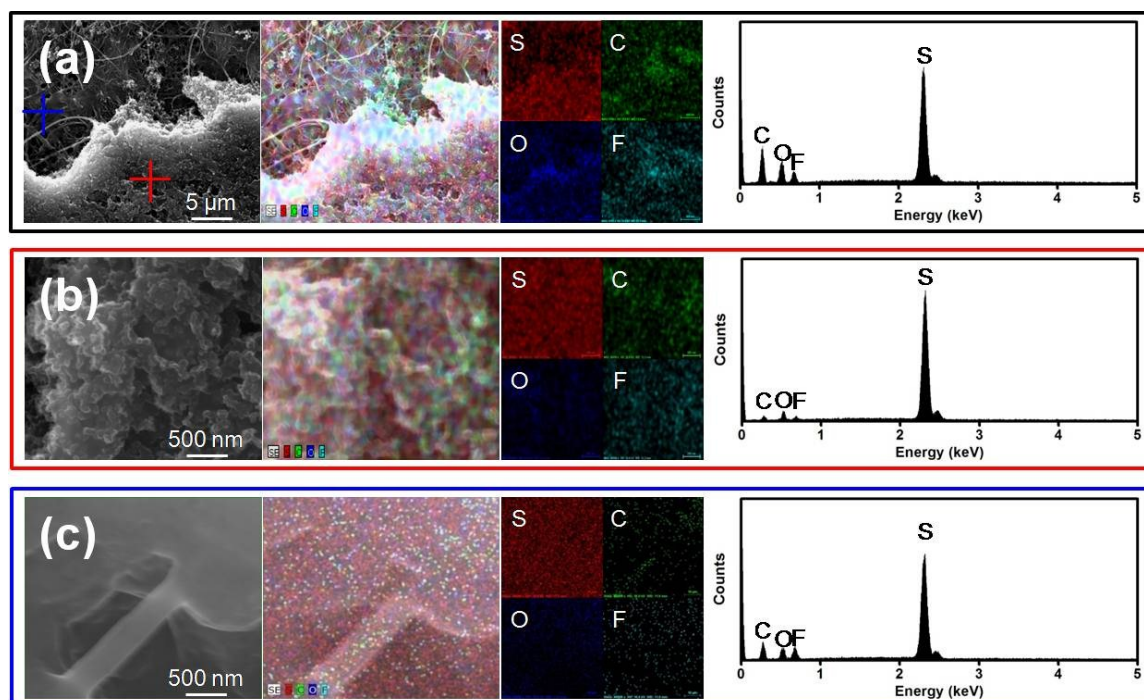


Fig. S8. Microstructural analysis: (a – c) low and high magnification SEM/EDX inspection of the cycled sulfur core. The cycled sulfur core in Fig. S8 has  $4 \text{ mg cm}^{-2}$  sulfur. The microstructural analysis is conducted after the cathodes have been cycled for 100 cycles and stopped at the charged state (3.0 V).

The cycled sulfur core shown in Fig. S8 is prepared by peeling off the upper carbon shell from a cycled core-shell cathode and then removing a part of active material from the sulfur core by a blade. It is evident that the cycled sulfur core arranges itself to occupying a more electrochemically favorable position, such as the small active-material particles and a more uniform surface morphology shown in Fig. S8b and the closer contact and better coverage between the active material and CNT/CNF matrix shown in Fig. S8c. These *in-situ* rearrangements of the active material promote the smooth ion and electron transport. It is notable that the prerequisite for a benign *in-situ* rearrangement is the excellent polysulfide retention. Otherwise, the polysulfide diffusion should only lead to a negative rearrangement, which causes the fast capacity fade and electrode degradation.

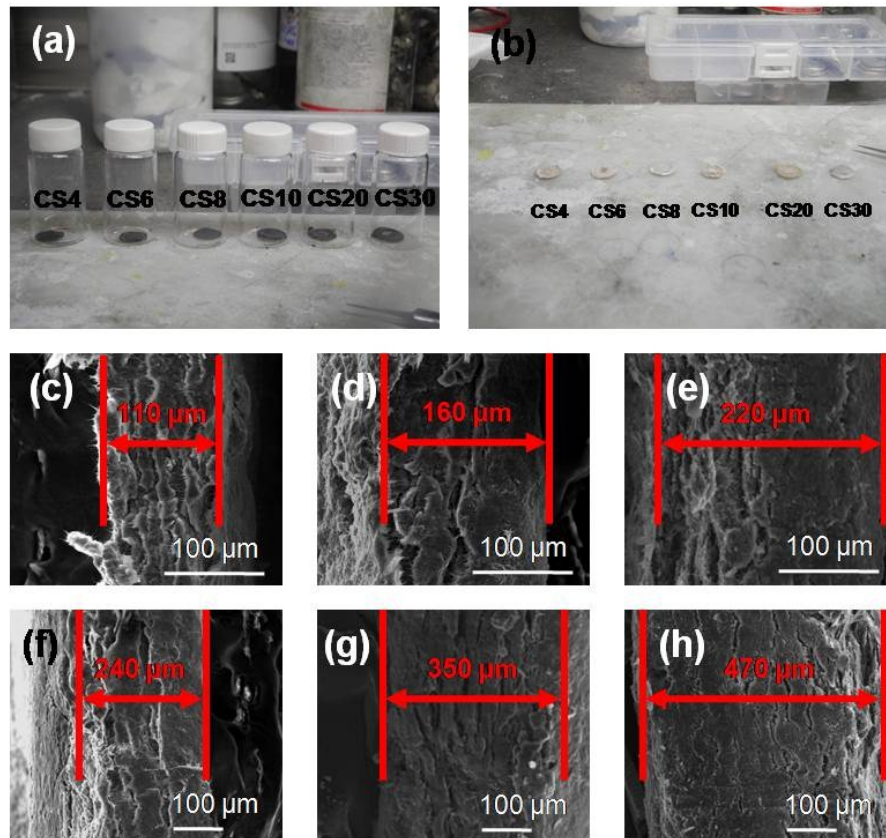


Fig. S9. Morphological and microstructural analysis: digital images of (a) cycled core-shell cathodes with various sulfur loadings and (b) the corresponding lithium anodes. Cross-sectional SEM inspection of the cycled core-shell cathodes with (c) 4 mg cm<sup>-2</sup>, (d) 6 mg cm<sup>-2</sup>, (e) 8 mg cm<sup>-2</sup>, (f) 10 mg cm<sup>-2</sup>, (g) 20 mg cm<sup>-2</sup>, and (h) 30 mg cm<sup>-2</sup> sulfur cores. The morphological and microstructural analyses were conducted after the electrodes have been cycled for 100 cycles and stopped at the charged state (3.0 V).

The cycled core-shell cathode shows no obvious deformations and damages. The good electrode integrity suggests the good flexibility and mechanical strength of the core-shell cathode, which could tolerate the volume change resulting from the high-loading sulfur cores and ensure the normal function of the Li-S cells. On the other hand, the corresponding cycled anodes retain good surface morphology with no severe deposition of the redox products. This might result from the direct lithium-metal stabilization from LiNO<sub>3</sub> co-salt and the indirect lithium-metal stabilization from the core-shell cathode.

Figs. S9c – h show the cross-sectional SEM images of the cycled core-shell cathodes with various sulfur loadings. As the sulfur loading increases, the areal and gravimetric capacities would be raised, but so would be the thickness. The increasing thickness of the electrodes would influence the volumetric capacity and could remain as a new challenge for high-loading sulfur cathodes.

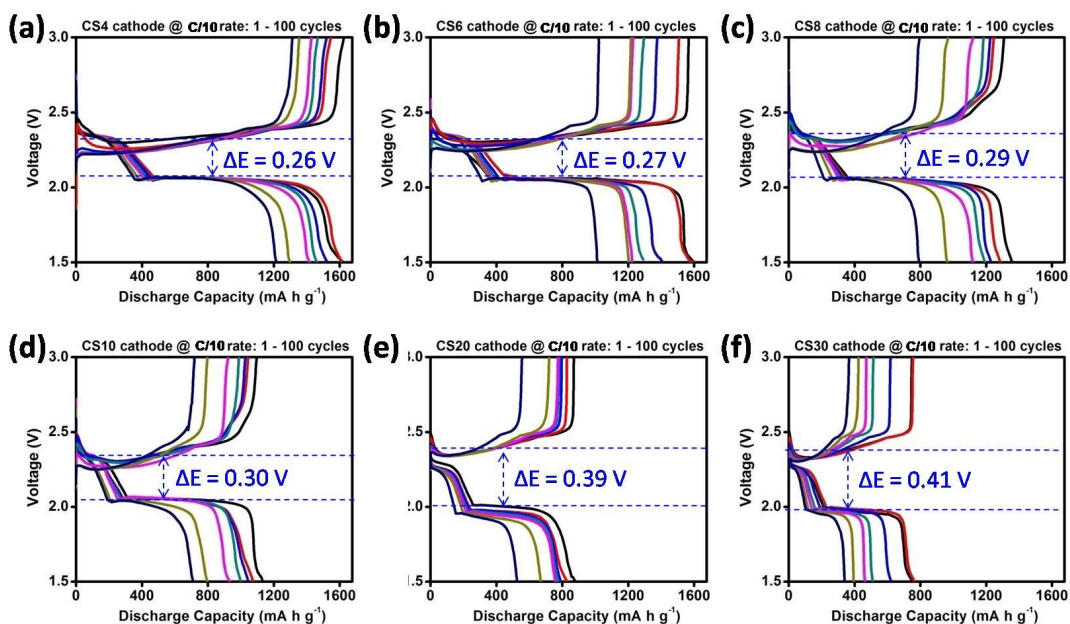


Fig. S10. Dynamic battery chemistries: discharge and charge profiles of the cells employing the core-shell cathodes with (a)  $4 \text{ mg cm}^{-2}$ , (b)  $6 \text{ mg cm}^{-2}$ , (c)  $8 \text{ mg cm}^{-2}$ , (d)  $10 \text{ mg cm}^{-2}$ , (e)  $20 \text{ mg cm}^{-2}$ , and (f)  $30 \text{ mg cm}^{-2}$  sulfur cores.

Fig. S10 summarizes the discharge and charge profiles for 100 cycles and shows the relationship between the increasing sulfur loadings and the electrochemical characteristics. First, the discharge and charge curves are overlapping and reveal no severe shrinkage. Such high electrochemical reversibility and stability confirm that the core-shell cathodes bring benefits on stabilizing the high-loading sulfur cathodes and the corresponding cell performance. Second, as the sulfur core loads with high amount of active material of  $4 \text{ mg cm}^{-2}$  and subsequently increases up to  $30 \text{ mg cm}^{-2}$ , which is also the highest sulfur loading ever reported, the polarization remains at a reasonably low value. This demonstrates the outstanding redox-reaction capability brought by the core-shell cathode configuration. In addition, the polarization level shows no obvious increase upon electrochemical cycling, a result of the limited polysulfide diffusion and the ensuing eliminated insulating  $\text{Li}_2\text{S}/\text{Li}_2\text{S}_2$  re-deposition on the electrode surface.

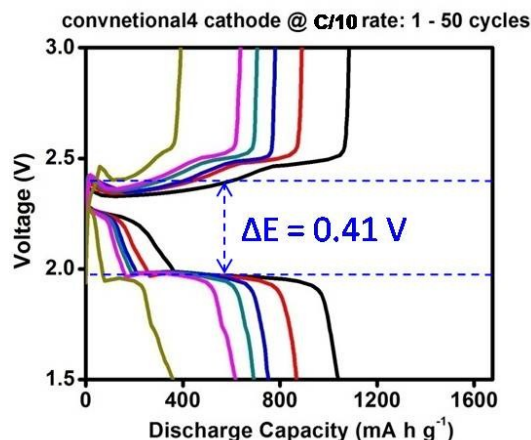


Fig. S11. Dynamic battery chemistries: discharge and charge profiles of the control cells employing the conventional cathode with  $4 \text{ mg cm}^{-2}$  sulfur.

As a reference, the control cell with a conventional sulfur cathode shows the evident shrinkage of the discharge and charge plateaus and the increasing polarization from 0.41 V. These disadvantages result from the polysulfide diffusion that causes the loss of active material and the degradation of the cathode, reflecting in a fast capacity fade in only 50 cycles. Subsequently, the diffusing polysulfides could re-deposit onto the electrode surface as the insulating  $\text{Li}_2\text{S}/\text{Li}_2\text{S}_2$  layer during cell cycling, which reduces the accessible reaction area of the cathode and increases the cathode resistance. Thus, an increasing polarization could be observed.

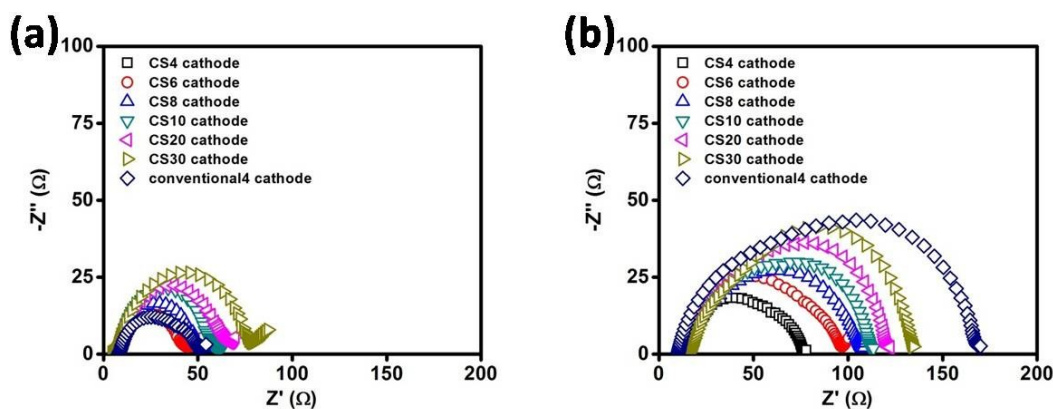


Fig. S12. Dynamic battery chemistries: EIS of the cells employing the core-shell cathodes with increasing sulfur loadings from  $4$  to  $30 \text{ mg cm}^{-2}$  and the conventional cathode with sulfur loading of  $4 \text{ mg cm}^{-2}$  (a) before and (b) after cycling.

Fig. S12 shows that the core-shell cathodes maintain a low cell resistance and exhibit limited increase in cell resistance even as the sulfur loading increases from  $4$  to  $30 \text{ mg cm}^{-2}$  after 100 cycles. In contrast, the conventional sulfur cathode ( $4 \text{ mg cm}^{-2}$ ) displays a significant increase in cell resistance in only 50 cycles, while it has the lowest sulfur loading.

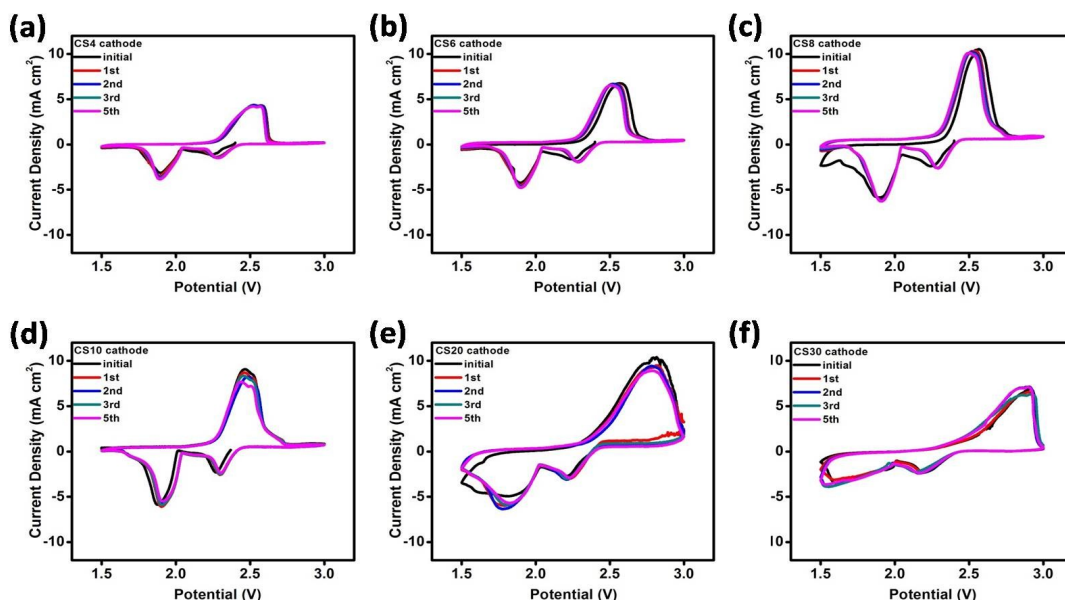


Fig. S13. Dynamic battery chemistries: cyclic voltammograms of the cells employing the core-shell cathodes with (a) 4 mg cm<sup>-2</sup>, (b) 6 mg cm<sup>-2</sup>, (c) 8 mg cm<sup>-2</sup>, (d) 10 mg cm<sup>-2</sup>, (e) 20 mg cm<sup>-2</sup>, and (f) 30 mg cm<sup>-2</sup> sulfur cores.

The enhanced electrochemical stability could also be illustrated by the overlapping curves of the cyclic voltammograms (CV). The overlapping CV curves of the core-shell cathodes that are equipped with high-loading sulfur cores attest to the superior cell reversibility and stability.

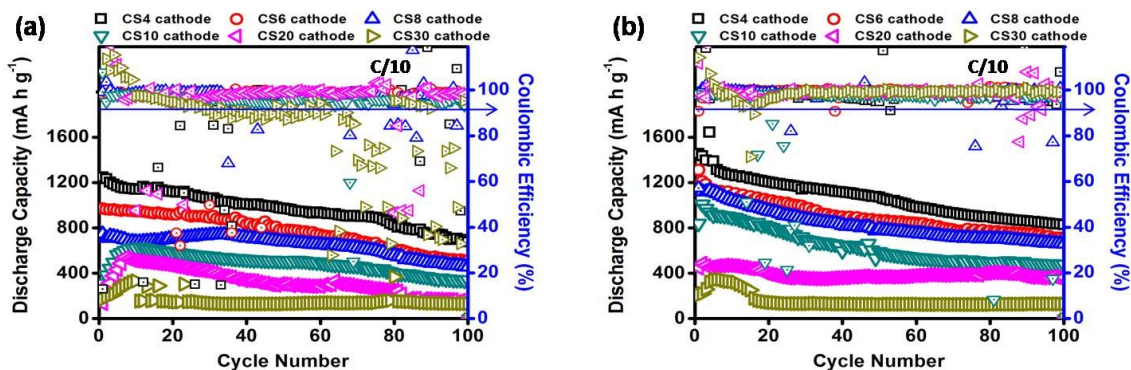


Fig. S14. Configuration of the core-shell cathode: battery performance of (a) the top-cover-free core-shell cathodes and (b) the o-ring-free core-shell cathodes with various sulfur loadings from 4 to 30 mg cm<sup>-2</sup> at C/10 rate.

In Fig. S14, the top-cover-free core-shell cathodes have the poorest cell cyclability, especially the high-loading performances. Without the top cover to block the migration of polysulfides, the active material is free to diffuse out from the high-loading sulfur core so that the polysulfide diffusion becomes severe. The cells employing the o-ring-free core-shell cathodes with sulfur loadings from 4 to 10 mg cm<sup>-2</sup> still show a good battery performance while capacity fade could be observed. As the high-loading sulfur cores are used in the cell, the active material might diffuse out from the cathodes due to the unblocked electrode edge and the use of a thick sulfur core.

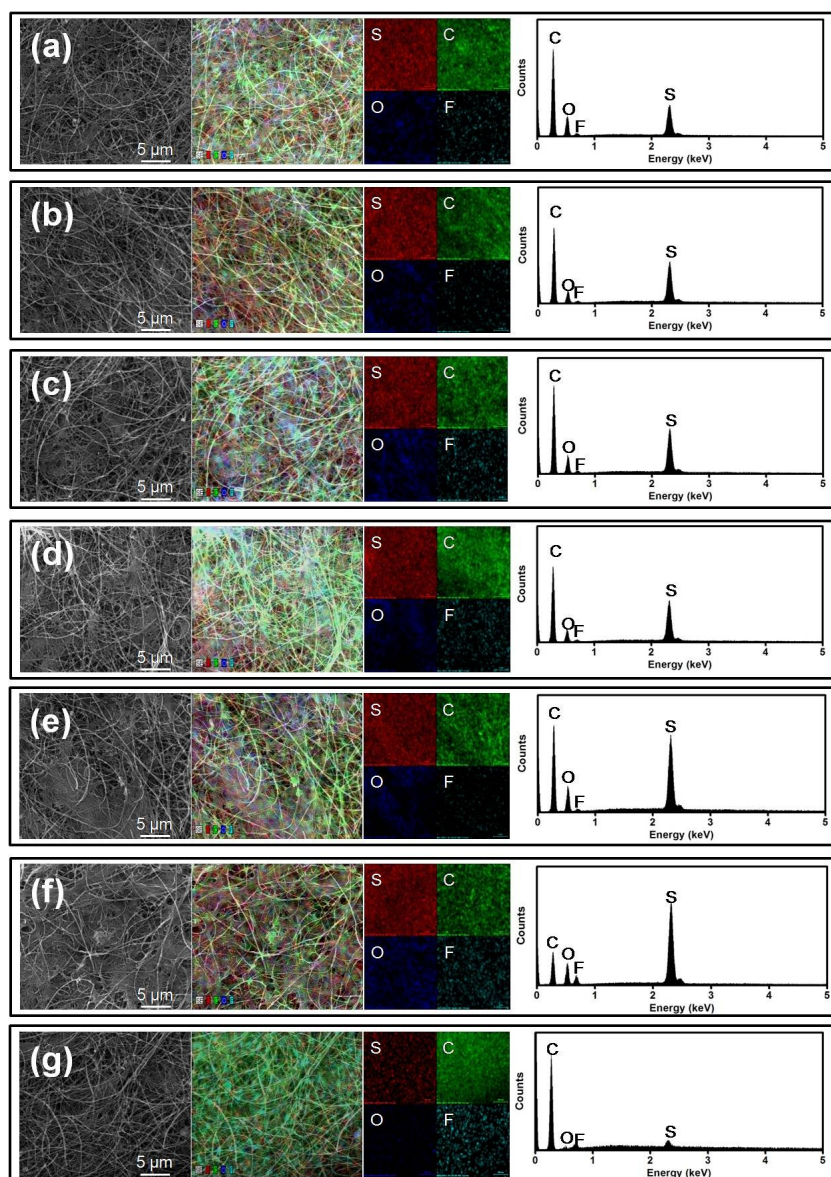


Fig. S15. Microstructural analysis: SEM/EDX inspection from the edge of the cycled o-ring-free core-shell cathodes with (a)  $4 \text{ mg cm}^{-2}$ , (b)  $6 \text{ mg cm}^{-2}$ , (c)  $8 \text{ mg cm}^{-2}$ , (d)  $10 \text{ mg cm}^{-2}$ , (e)  $20 \text{ mg cm}^{-2}$ , and (f)  $30 \text{ mg cm}^{-2}$  sulfur cores. (g) SEM/EDX inspection from the edge of the cycled core-shell cathode with a  $30 \text{ mg cm}^{-2}$  sulfur core. The microstructural analysis was conducted after the cathodes have been cycled for 100 cycles and stopped at the charged state (3.0 V).

In Fig. S15a – f, the SEM/EDX inspection from the edge of the o-ring-free core-shell electrodes reveals obvious morphological changes and strong sulfur signals. The ratio of the sulfur signal to carbon signal increases when the sulfur loading increases. This evidences that the polysulfides could escape out from the o-ring-free core-shell cathode via the open electrode edge, especially when the sulfur loading increases. As a comparison, in Figs. S6 and S15g, the experimental cells employing the standard core-shell cathodes with various sulfur loadings exhibit limited elemental sulfur signals at the edge of the core-shell cathode.

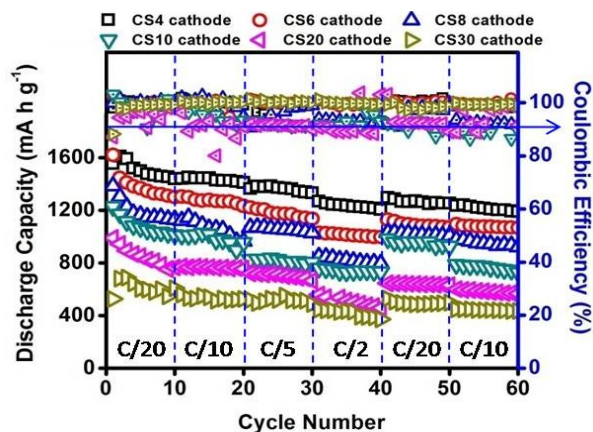


Fig. S16. Dynamic battery chemistries: rate capability of the cells employing the core-shell cathodes with increasing sulfur loadings at C/20 – C/2 rates.

As a supporting data for Fig. 3, Fig. S16 attests to the outstanding rate capability by showing the stable cyclability and reversible capacity at various cycling rates with another cycling method.

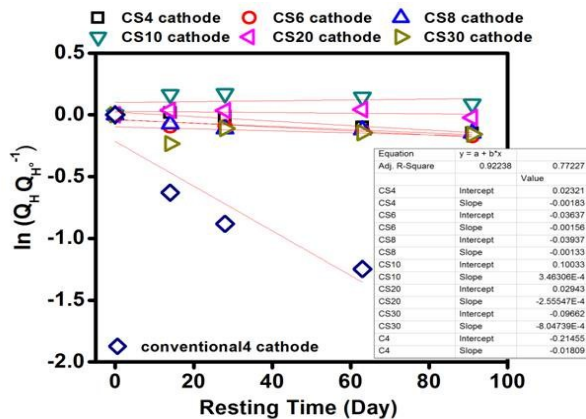


Fig. S17. Static battery chemistries: natural logarithm of upper-plateau discharge capacity ( $Q_H$ ) divided by the original upper-plateau discharge capacity ( $Q_{H0}$ ) as a function of resting time ( $T_R$ ) for self-discharge constant calculation (the inset is the self-discharge constant fitting).

The core-shell cathodes with increasing sulfur loadings of 4, 6, 8, 10, 20, and 30 mg cm<sup>-2</sup><sub>S</sub> show the low  $K_S$  values of, respectively, 0.0018, 0.0016, 0.0013, 0.0003, 0.0003, and 0.0008 day<sup>-1</sup>, which are the lowest  $K_S$  values compared to other self-discharge values reported in the literature for Li-S cells.<sup>15,55-63</sup> The low  $K_S$  value provides quantitative evaluation that the core-shell cathode functions excellently as a containment building, stabilizing the sulfur core and keeping the active material from dissolving into the electrolyte during long-term storage. In contrast, the  $K_S$  value of the conventional cathode is as high as 0.0181 day<sup>-1</sup>. The high  $K_S$  value implies that the conventional sulfur cathode configuration has inevitable, severe self-discharge effect.

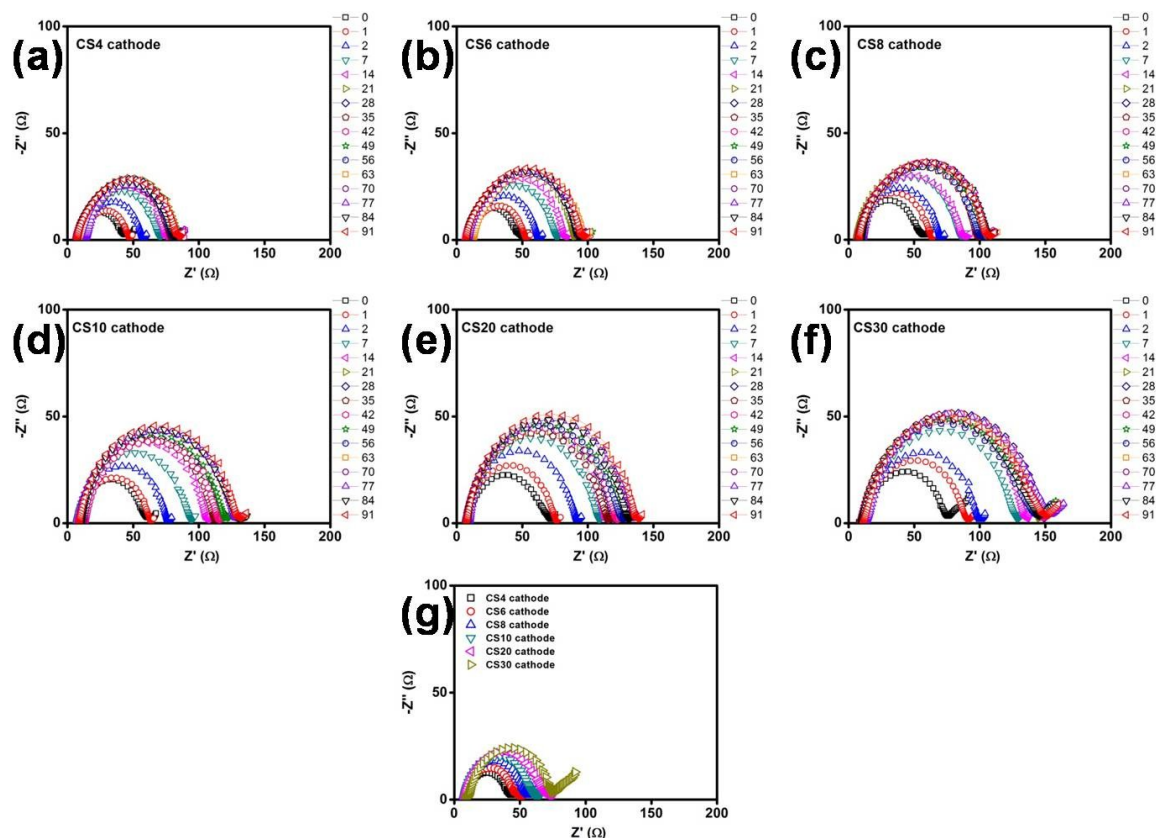


Fig. S18. Static battery chemistries: time-dependent EIS of the cells employing the core-shell cathodes with (a) 4 mg cm<sup>-2</sup>, (b) 6 mg cm<sup>-2</sup>, (c) 8 mg cm<sup>-2</sup>, (d) 10 mg cm<sup>-2</sup>, (e) 20 mg cm<sup>-2</sup>, and (f) 30 mg cm<sup>-2</sup> sulfur cores after a three-month rest period. (g) Time-dependent EIS of the cells employing the core-shell cathodes before resting.

Time-dependent EIS is measured for the investigation of the electrode reactions during cell resting. Fig. S18 shows, in general, a slight increase in cell impedance during the initial 14-day rest period and then shows stable impedance in the following rest period. The steady cell resistance indicates the stable static electrode reactions, a result of the limited sulfur-to-polysulfide conversion and the ensuing suppressed polysulfide diffusion and eliminated Li<sub>2</sub>S/Li<sub>2</sub>S<sub>2</sub> re-deposition during cell resting.

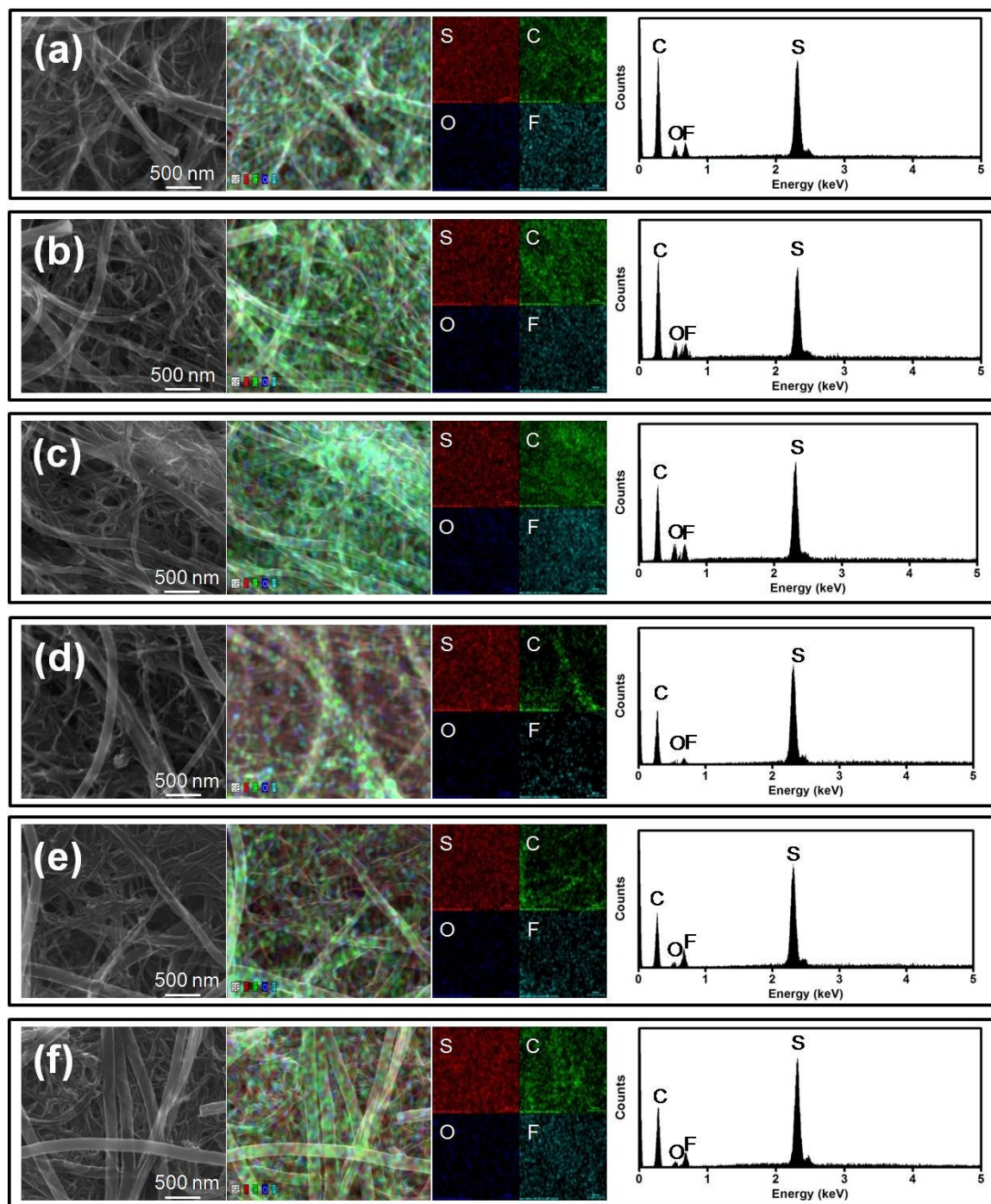


Fig. S19. Static battery chemistries: SEM/EDX inspection from the core-shell cathodes with (a)  $4 \text{ mg cm}^{-2}$ , (b)  $6 \text{ mg cm}^{-2}$ , (c)  $8 \text{ mg cm}^{-2}$ , (d)  $10 \text{ mg cm}^{-2}$ , (e)  $20 \text{ mg cm}^{-2}$ , and (f)  $30 \text{ mg cm}^{-2}$  sulfur cores after resting for a three-month rest period.

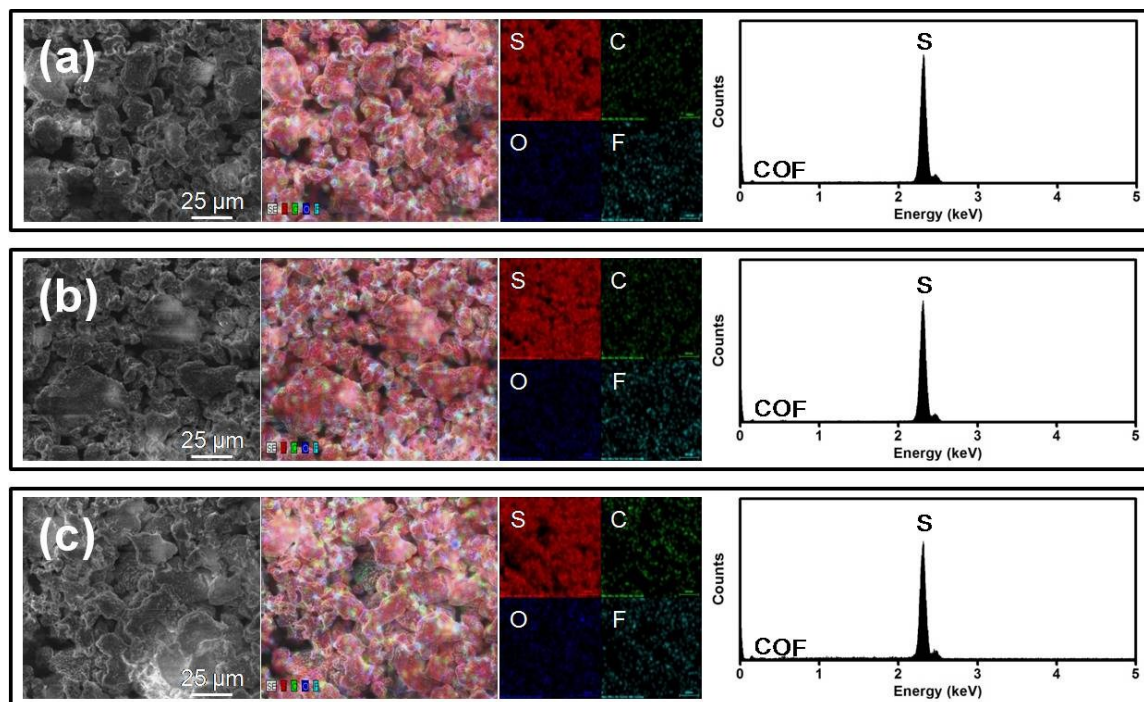


Fig. S20. Static battery chemistries: SEM/EDX inspection from the sulfur cores after resting for a (a) one-, (b) two-, and (c) three-month rest period. The sulfur cores have the same sulfur loadings of 4 mg cm<sup>-2</sup>.

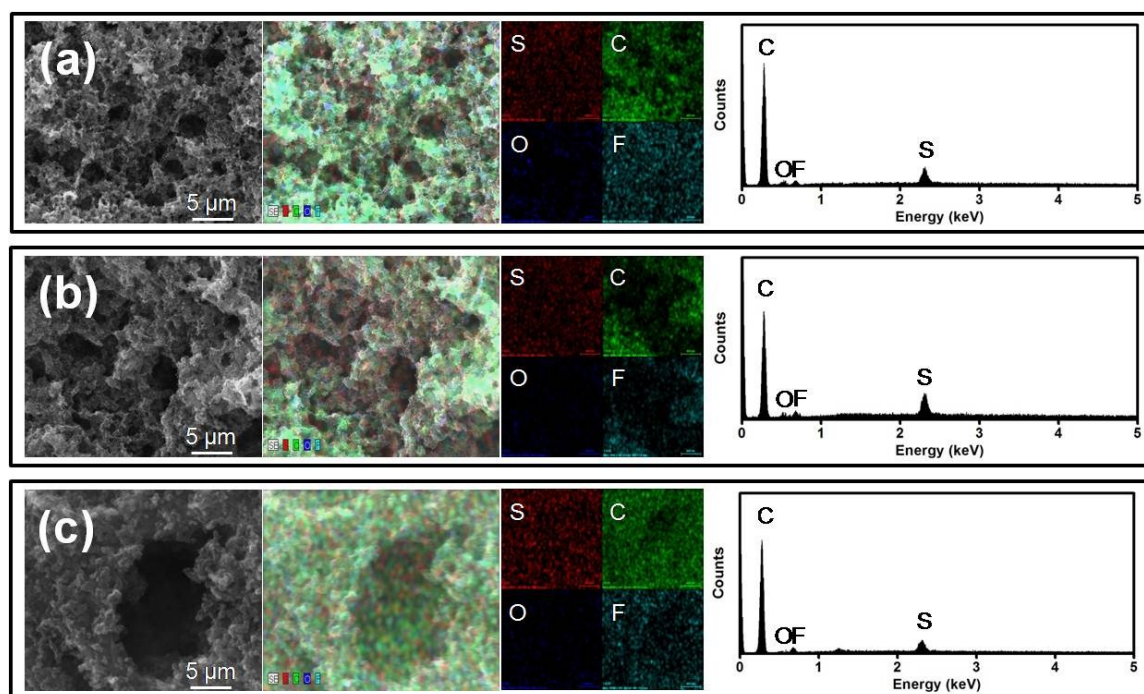


Fig. S21. Static battery chemistries: SEM/EDX inspection from the conventional sulfur cathodes after resting for a (a) one-, (b) two-, and (c) three-month rest period. The sulfur loading is 4 mg cm<sup>-2</sup>.

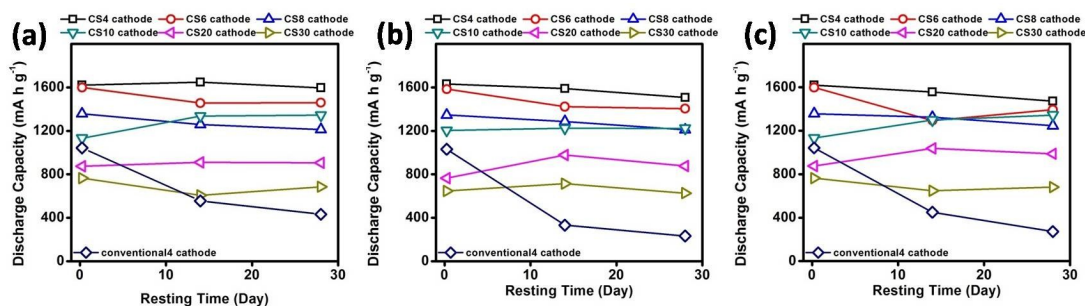


Fig. S22. Static battery chemistries: self-discharge behavior of Li-S cells employing the core-shell cathodes with various sulfur loadings from 4 to 30 mg cm<sup>-2</sup> under different cell storage conditions: (a) uncycled state (OCV), (b) half-discharged state (2.15 V), and (c) fully-discharged state (1.5 V).

The cells resting at the uncycled state aim to reflect the possible chemical reactions during cell resting (Fig. S22a). The cells resting at the half-discharged state are expected to reflect a clear self-discharge effect due to (i) the formation of high polysulfide content and (ii) the ensuing uncontrollable polysulfide migration in the cell during cell storage (Fig. S22b). The cells resting at the fully-discharged state exhibit the redox chemistry impacted by the formation of insulating and electrochemically inactive Li<sub>2</sub>S<sub>2</sub>/Li<sub>2</sub>S mixtures, which might reduce the electrochemical accessibility and slow down the redox kinetics (Fig. S22c).

In comparison to Figs. 5 and S22a, in Fig. S22b and c, the control cells using conventional cathodes exhibit severe self-discharge at both half- and fully-discharged states, a result of the free migration of the high-content polysulfides and the reduced electrochemical activity of the cathodes. In contrast, at different cell-storage conditions, the experimental cells employing the core-shell cathodes retain the high original capacity, reflecting the low self-discharge effect. This implies that shell-shaped electrode could suppress the unwanted sulfur dissolution, polysulfide diffusion, and electrode degradation during cell resting.

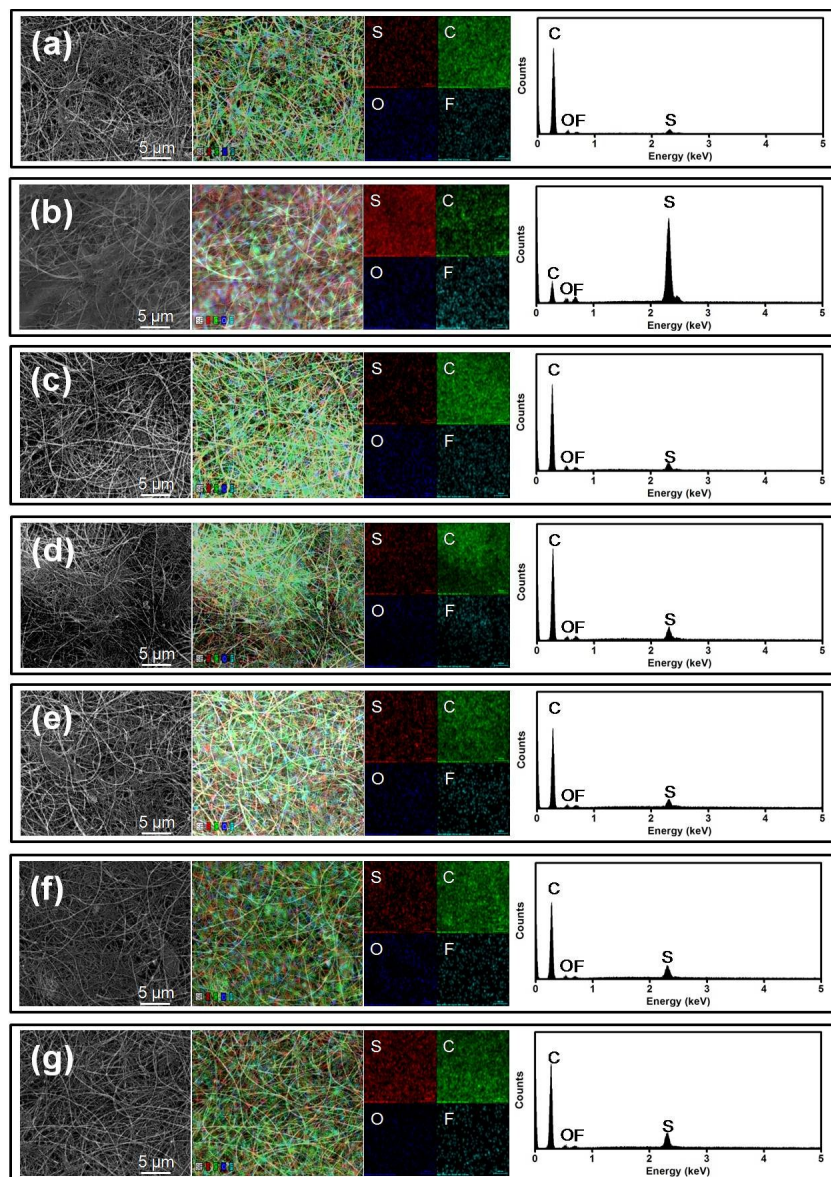


Fig. S23. Polysulfide-trap cell testing: SEM/EDX inspection of the cyclized polysulfide traps from the (a) experimental cells employing the core-shell cathode and (b) control cells employing the conventional sulfur cathode. Both cathodes have  $4 \text{ mg cm}^{-2}$  sulfur. SEM/EDX inspection of the cyclized polysulfide traps from the experimental cells employing the core-shell cathodes with (c)  $6 \text{ mg cm}^{-2}$ , (d)  $8 \text{ mg cm}^{-2}$ , (e)  $10 \text{ mg cm}^{-2}$ , (f)  $20 \text{ mg cm}^{-2}$ , and (g)  $30 \text{ mg cm}^{-2}$  sulfur cores after 100 cycles.

The SEM/EDX inspection in Fig. S23a and b shows the cyclized polysulfide trap from experimental and control cells. The experimental cells employing the core-shell cathodes show no redox products on their cyclized traps. In contrast, the control cell shows high amount of sulfur-containing species on the cyclized trap. This demonstrates the superior polysulfide-retention capability of the core-shell cathode. Fig. S23c – g also shows low trapped active material and so confirms the superior polysulfide retention of core-shell cathodes with increasing sulfur loadings.

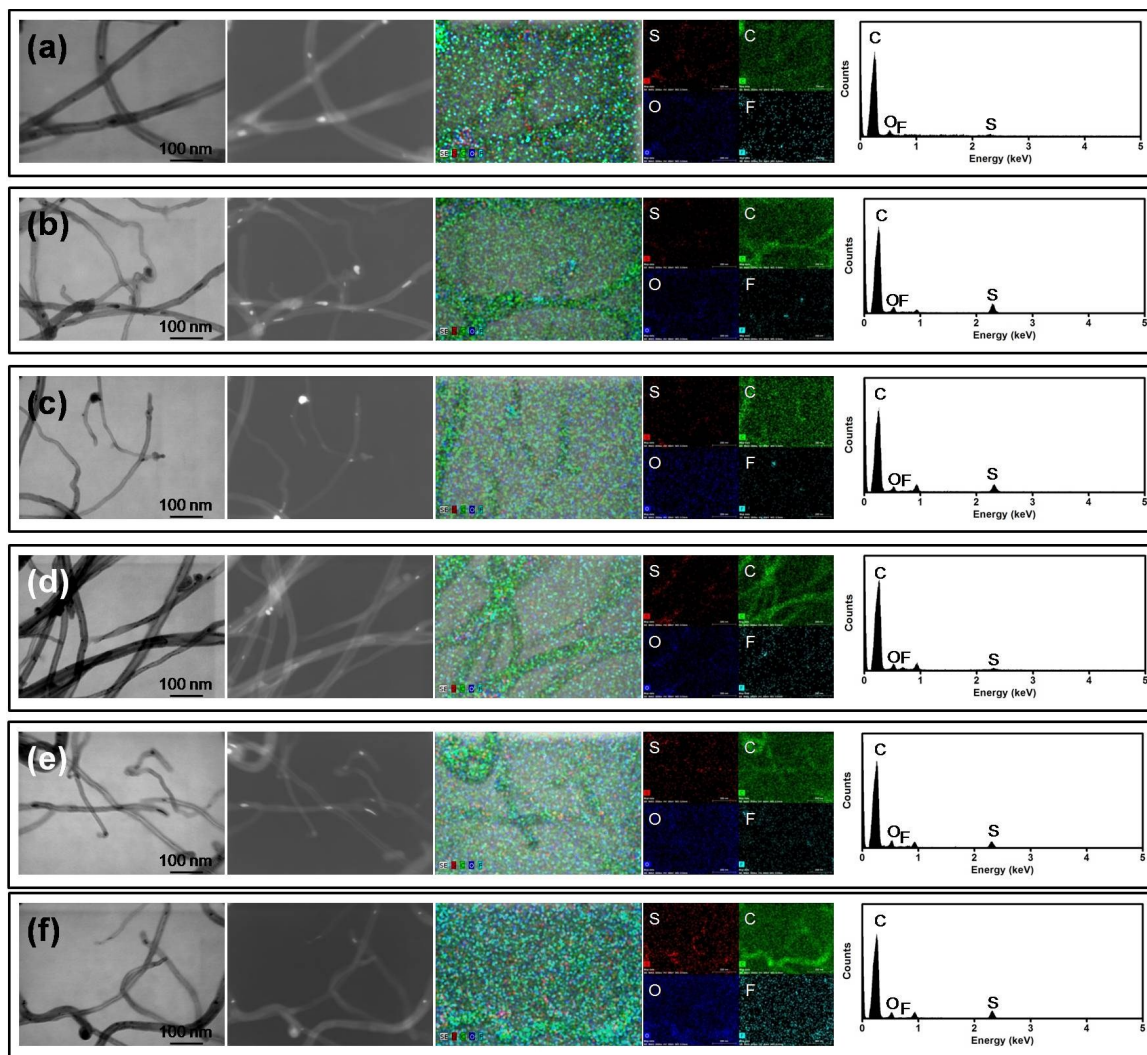


Fig. S24. Polysulfide-trap cell testing: STEM/EDX inspection of the cycled polysulfide traps from the experimental cells employing the core-shell cathodes with (a)  $4 \text{ mg cm}^{-2}$ , (b)  $6 \text{ mg cm}^{-2}$ , (c)  $8 \text{ mg cm}^{-2}$ , (d)  $10 \text{ mg cm}^{-2}$ , (e)  $20 \text{ mg cm}^{-2}$ , and (f)  $30 \text{ mg cm}^{-2}$  sulfur cores after 100 cycles.

The STEM/EDX inspection of the cycled polysulfide traps display no redox products covering on the CNT/CNF networks (BF-/DF-STEM) as well as the weak elemental sulfur signals in the EDX spectra and mapping results. These characteristics confirm that the core-shell cathode configuration is able to eliminate the severe polysulfide diffusion.

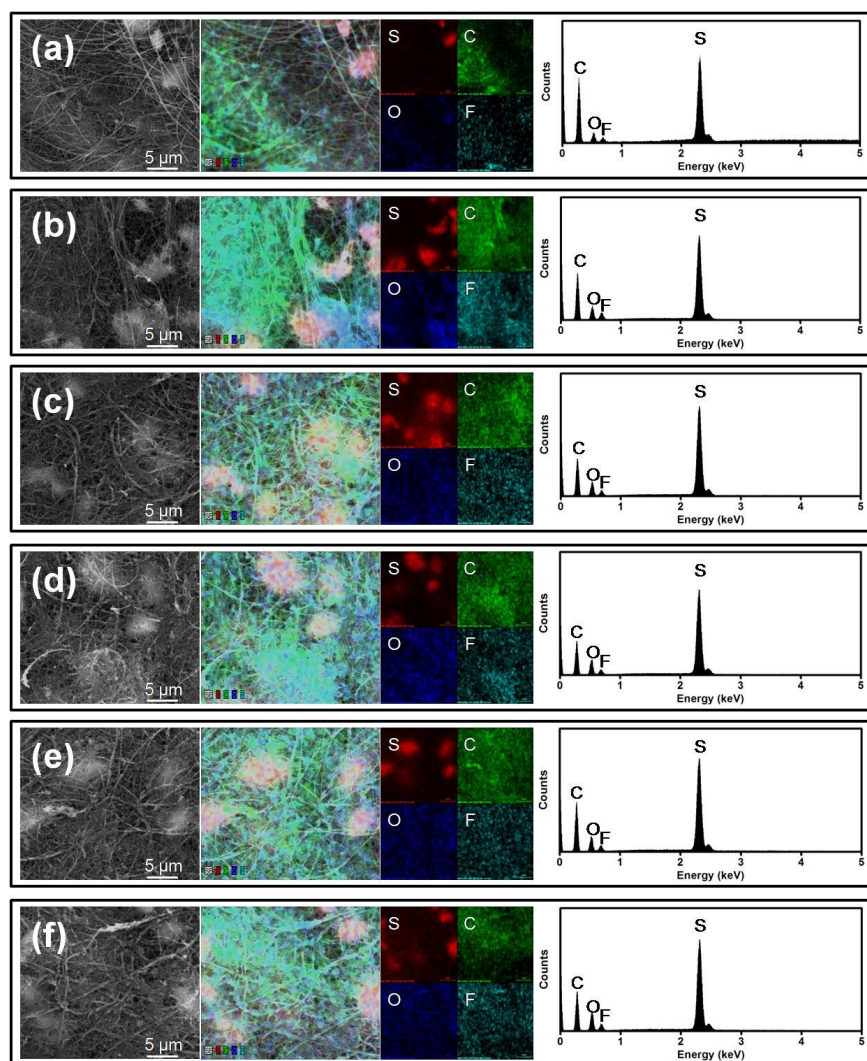


Fig. S25. Polysulfide-trap cell testing: SEM/EDX inspection of the cyclized polysulfide trap from the cells employing the top-cover-free core-shell cathode with (a) 4 mg cm<sup>-2</sup>, (b) 6 mg cm<sup>-2</sup>, (c) 8 mg cm<sup>-2</sup>, (d) 10 mg cm<sup>-2</sup>, (e) 20 mg cm<sup>-2</sup>, and (f) 30 mg cm<sup>-2</sup> sulfur cores after 100 cycles.

The SEM/EDX inspection in Fig. S25 shows the cyclized polysulfide traps retrieved from the experimental cells that employ the top-cover-free core-shell cathodes. The shell-shaped electrode without a top cover functions as a porous current collector, which stores the active material within its porous network. However, without a top cover to trap the dissolved polysulfides, the experimental cells show obvious redox products deposited on their cyclized traps. The relative intensity of elemental sulfur EDX peaks increases as the sulfur loading increases. The high amount of trapped active material forms visible clusters composed of sulfur-containing species. The results show the importance of the top cover in blocking the polysulfide migration and, therefore, confirm the polysulfide-retention capability of core-shell cathodes.

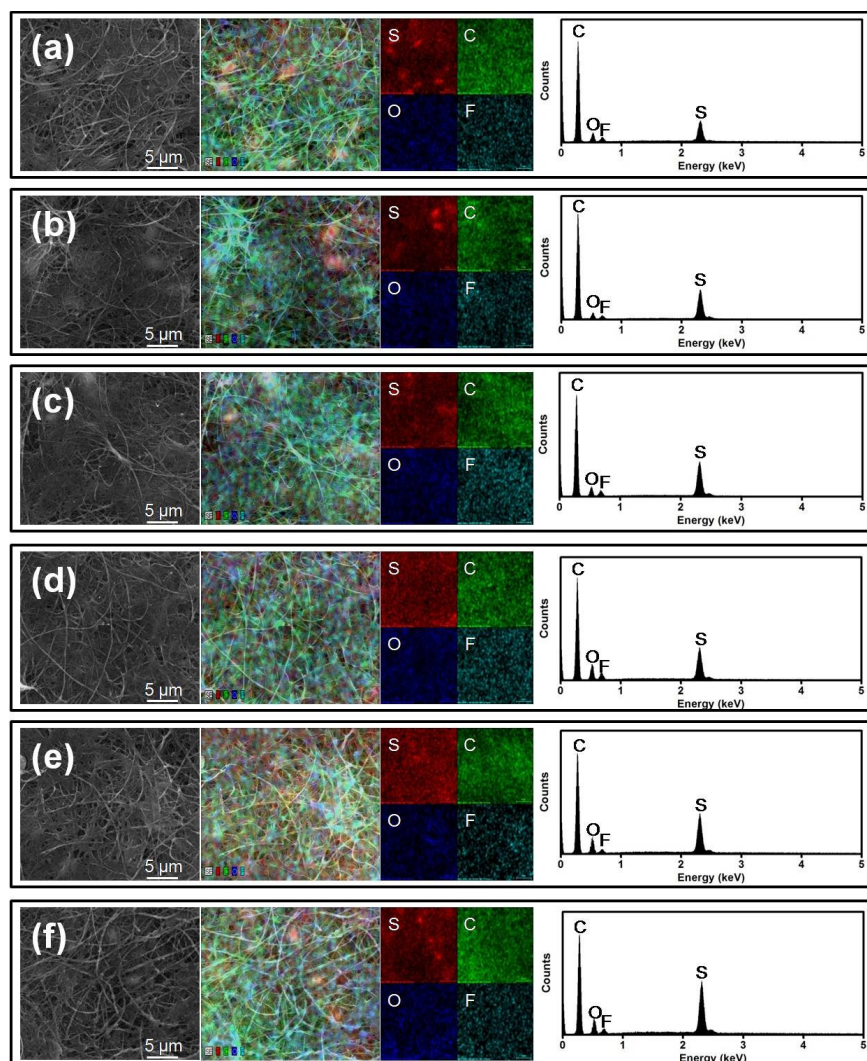


Fig. S26. Polysulfide-trap cell testing: SEM/EDX inspection of the cyclized polysulfide traps from the cells employing the o-ring-free core-shell cathodes with (a)  $4 \text{ mg cm}^{-2}$ , (b)  $6 \text{ mg cm}^{-2}$ , (c)  $8 \text{ mg cm}^{-2}$ , (d)  $10 \text{ mg cm}^{-2}$ , (e)  $20 \text{ mg cm}^{-2}$ , and (f)  $30 \text{ mg cm}^{-2}$  sulfur cores after 100 cycles.

The shell-shaped electrodes without an o-ring function similar to a sandwiched cathode and show stable cell performances. However, the lack of the o-ring still leads to polysulfide diffusion through the open edge of the cathode. This causes capacity fade and leads to poor cycling performance of the cells with sulfur loadings above  $20 \text{ mg cm}^{-2}$ , as shown in Fig. S14b. The polysulfide diffusion from the edge of the cathode was evidenced in Fig. S15. As supporting data, in Fig. S26, the SEM/EDX inspection shows the cyclized polysulfide traps from the experimental cells that employ the o-ring-free core-shell cathodes. The elemental analysis evidence the inevitable polysulfide diffusion from the o-ring-free core-shell cathodes. These microstructural analyses could conclude that in order to avoid the inevitable polysulfide diffusion from the edge of the cathode, the intact core-shell cathode could be a practical electrode design.

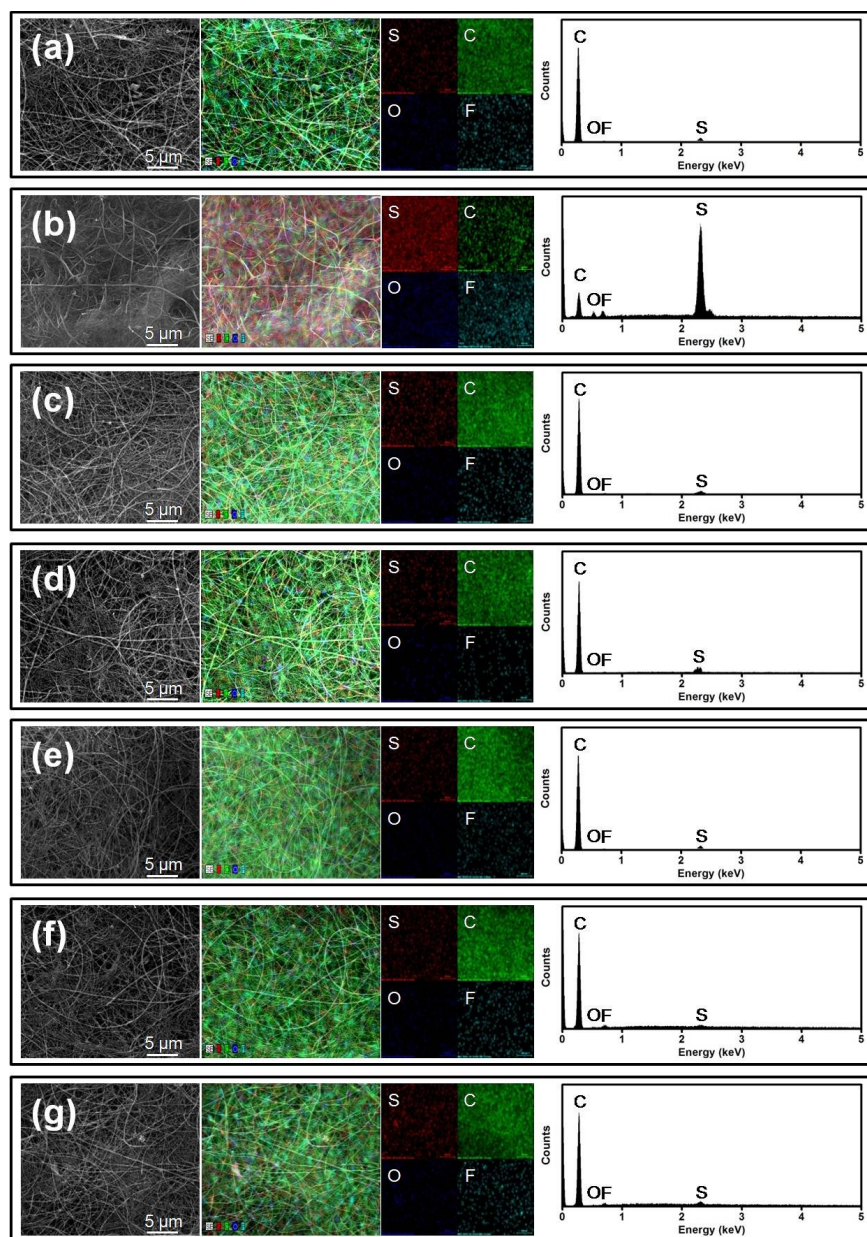


Fig. S27. Polysulfide-trap cell testing: SEM/EDX inspection of the polysulfide traps from the (a) experimental cells employing the core-shell cathodes and (b) control cells employing the conventional sulfur cathode after a three-month rest period. Both cathodes have  $4 \text{ mg cm}^{-2}$  sulfur. SEM/EDX inspection of the polysulfide trap from the experimental cells employing the core-shell cathode with (c)  $6 \text{ mg cm}^{-2}$ , (d)  $8 \text{ mg cm}^{-2}$ , (e)  $10 \text{ mg cm}^{-2}$ , (f)  $20 \text{ mg cm}^{-2}$ , and (g)  $30 \text{ mg cm}^{-2}$  sulfur cores after a three-month rest period.

The SEM/EDX inspections in Fig. S27 show that the results of static polysulfide-trap experiments are similar to those in Fig. S23 for the dynamic cases. Fig. S27 affirms the outstanding polysulfide retention of the core-shell cathodes with increasing sulfur loadings and the severe polysulfide diffusion of the conventional cathodes during cell resting.

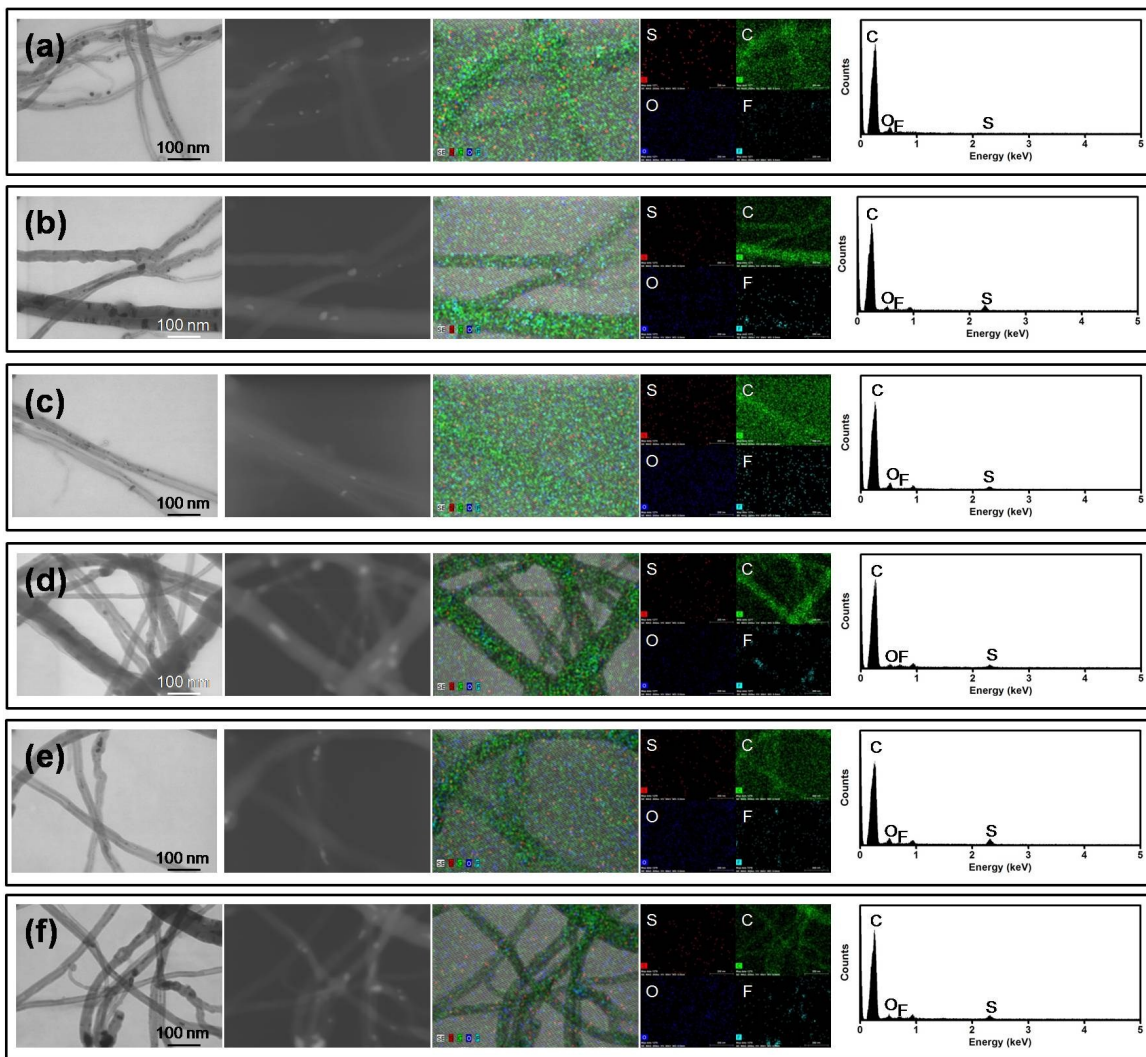


Fig. S28. Polysulfide-trap cell testing: STEM/EDX inspection of the polysulfide traps from the experimental cells employing the core-shell cathodes with (a) 4 mg cm<sup>-2</sup>, (b) 6 mg cm<sup>-2</sup>, (c) 8 mg cm<sup>-2</sup>, (d) 10 mg cm<sup>-2</sup>, (e) 20 mg cm<sup>-2</sup>, and (f) 30 mg cm<sup>-2</sup> sulfur cores after a three-month rest period.

The STEM/EDX inspection of the polysulfide traps after a three-month rest period also displays no redox products covering on the CNT/CNF networks as shown in the BF-/DF-STEM images, as well as the weak elemental sulfur signals in EDX spectra and mapping results. These characteristics confirm that the core-shell cathode configuration is able to eliminate the severe self-discharge.

Table S1. Cathode fabrication parameters

Parameters	Sulfur loading [mg cm <sup>-2</sup> ]	Sulfur mass [mg electrode <sup>-1</sup> ]	Sulfur content [%] / [%]*	Electrode thickness [ $\mu$ m]
CS4 cathode	4.0	4.0	45.45 / 45.45*	110
conventional4 cathode	4.0	4.0	70.00 / 37.81*	105
sulfur cores with increasing active-material loadings				
CS6 cathode	6.0	6.0	51.72 / 51.72*	160
CS8 cathode	8.0	8.0	55.56 / 55.56*	220
CS10 cathode	10.0	10.0	58.14 / 58.14*	240
CS20 cathode	20.0	20.0	65.79 / 65.79*	350
CS30 cathode	30.0	30.0	68.81 / 68.81*	470
Sulfur content [%]*: The calculation includes everything in the cathode region				

Table S2. Analytical results of Q<sub>H</sub> and Q<sub>L</sub> calculation

Parameters	Q <sub>H</sub> utilization rate [%]	Q <sub>L</sub> utilization rate [%]	Q <sub>H</sub> retention rate [%]	Q <sub>L</sub> retention rate [%]
CS4 cathode	98.73	96.02	86.05	71.38
conventional4 cathode*	88.71	53.41	20.82	42.55
sulfur cores with increasing active-material loadings				
CS6 cathode	96.83	94.93	77.38	58.59
CS8 cathode	93.68	76.79	59.25	58.10
CS10 cathode	75.02	65.11	64.99	61.89
CS20 cathode	66.71	47.38	55.03	62.34
CS30 cathode	52.60	43.21	49.05	42.43
conventional4 cathode*: The Q <sub>H</sub> and Q <sub>L</sub> calculation of conventional4 cathodes is based on the control cell after 50 cycles. The analysis of core-shell cathodes is based on the experimental cells after 100 cycles.				

Table S3. Electrochemical data of the core-shell cathodes with increasing sulfur loadings at various cycling rates.

at C/20 rate (50 cycles)	Peak discharge capacity [mA h g <sup>-1</sup> ]	Reversible discharge capacity [mA h g <sup>-1</sup> ]	Capacity retention rate [%] (capacity fade rate [%])
sulfur cores with increasing active-material loadings			
CS4 cathode	1632	1267	77.60 (0.22 cycle <sup>-1</sup> )
CS6 cathode	1548	1122	72.44 (0.25 cycle <sup>-1</sup> )
CS8 cathode	1472	1019	69.22 (0.27 cycle <sup>-1</sup> )
CS10 cathode	1300	935	71.89 (0.22 cycle <sup>-1</sup> )
CS20 cathode	910	612	67.27 (0.18 cycle <sup>-1</sup> )
CS30 cathode	673	496	73.62 (0.11 cycle <sup>-1</sup> )
In order to show a fair comparison, the calculations of the capacity retention and fade			

rates are based on the peak capacities.

at C/10 rate (100 cycles)	Peak discharge capacity [mA h g <sup>-1</sup> ]	Reversible discharge capacity [mA h g <sup>-1</sup> ]	Capacity retention rate [%] (capacity fade rate [%])
CS4 cathode	1620	1218	75.17 (0.24 cycle <sup>-1</sup> )
conventional4 cathode*	1042	362	34.77 (0.41 cycle <sup>-1</sup> )
sulfur cores with increasing active-material loadings			
CS6 cathode	1598	1013	63.34 (0.35 cycle <sup>-1</sup> )
CS8 cathode	1357	793	58.43 (0.34 cycle <sup>-1</sup> )
CS10 cathode	1132	711	62.74 (0.25 cycle <sup>-1</sup> )
CS20 cathode	875	525	60.00 (0.21 cycle <sup>-1</sup> )
CS30 cathode	765	340	44.37 (0.25 cycle <sup>-1</sup> )
In order to show a fair comparison, the calculations of the capacity retention and fade rates are based on the peak capacities. conventional4 cathode*: The calculation of conventional4 cathodes is based on the control cell after 50 cycles. The analysis of core-shell cathodes is based on the experimental cells after 100 cycles.			

at C/5 rate (100 cycles)	Peak discharge capacity [mA h g <sup>-1</sup> ]	Reversible discharge capacity [mA h g <sup>-1</sup> ]	Capacity retention rate [%] (capacity fade rate [%])
sulfur cores with increasing active-material loadings			
CS4 cathode	1622	1134	69.89 (0.29 cycle <sup>-1</sup> )
CS6 cathode	1399	1035	73.98 (0.22 cycle <sup>-1</sup> )
CS8 cathode	1174	804	68.42 (0.23 cycle <sup>-1</sup> )
CS10 cathode	1090	743	68.08 (0.21 cycle <sup>-1</sup> )
CS20 cathode	867	643	74.20 (0.14 cycle <sup>-1</sup> )
CS30 cathode	774	423	54.56 (0.22 cycle <sup>-1</sup> )
In order to show a fair comparison, the calculations of the capacity retention and fade rates are based on the peak capacities.			

at C/2 rate (100 cycles)	Peak discharge capacity [mA h g <sup>-1</sup> ]	Reversible discharge capacity [mA h g <sup>-1</sup> ]	Capacity retention rate [%] (capacity fade rate [%])
sulfur cores with increasing active-material loadings			
CS4 cathode	1274	1037	81.35 (0.16 cycle <sup>-1</sup> )
CS6 cathode	1052	907	86.16 (0.09 cycle <sup>-1</sup> )
CS8 cathode	1017	667	65.59 (0.22 cycle <sup>-1</sup> )
CS10 cathode	885	674	76.12 (0.16 cycle <sup>-1</sup> )
CS20 cathode	636	464	72.91 (0.13 cycle <sup>-1</sup> )
CS30 cathode	526	340	64.60 (0.15 cycle <sup>-1</sup> )
In order to show a fair comparison, the calculations of the capacity retention and fade rates are based on the peak capacities.			

